Composites Part B 125 (2017) 9–18

Contents lists available at ScienceDirect

Composites Part B

journal homepage: www.elsevier.com/locate/compositesb

Anisotropy and holes in epoxy composite reinforced by carbon/glass and carbon/aramid hybrid fabrics: Experimental and analytical results

A.C.M.C. Batista [a, *], S.R.L. Tinô [a, b], R.S. Fontes [a], S.H.S. Nóbrega [a], E.M.F. Aquino [a, b]

[a] UFRN-Postgraduate Program in Mechanical Engineering, Technology Center, Natal, Rio Grande do Norte, Brazil
[b] UFRN-Postgraduate Program in Materials Science and Engineering, Campus Universitário, Lagoa Nova, Natal, Brazil

ARTICLE INFO

Article history:
Received 20 December 2016
Received in revised form
12 April 2017
Accepted 21 May 2017
Available online 25 May 2017

Keywords:
Fabrics
Analytical modeling
Mechanical testing
Epoxy vinyl ester resin

ABSTRACT

This study is based on research into the effect of anisotropy and the presence of holes on mechanical properties and final fracture characteristics in uniaxial tensile testing of two laminates, one using a carbon/glass fiber hybrid fabric and the other a carbon/aramid fiber hybrid fabric in loading directions at 0°, 90° and ±45°. Both laminates were impregnated with epoxy vinyl ester thermosetting resin (Derakane Momentum™ 411-350). An analytical study assesses stress concentration using the Point Stress Criterion (**PSC**) and Average Stress Criterion (**ASC**). The results show the direct influence of anisotropy, holes and residual properties on all the parameters studied. With respect to failure theories, both **PSC** and **ASC** showed good agreement when the geometric K value was used.

1. Introduction

The structural application of hybrid polymer composites has been increasing steadily, requiring better knowledge of the mechanical performance of these materials. Extensive studies have generally shown that the hybridization process is one of the most effective methods to regulate composite properties [1]. The hybridization was used in composites that use natural fibers [2–7] as reinforcement and composites that use synthetic fibers as reinforcement, such as glass, aramid and carbon [1,8–15]. Most of these studies involve the hybridization process, including several relevant investigations using hybrid composites, primarily those composed of different layers of interconnected fibers in a matrix. These materials may exhibit geometric discontinuities such as holes and notches, among others, and it is extremely important to understand their behavior. Drilling stands out as the most widely used operation in the machining of fiber-reinforced materials, due to the need to join structures [16].

Among the most important studies on the influence of geometric discontinuity in polymer hybrid composites, it can be highlighted papers that shows analysis of residual properties (Residual Strength and Residual Modulus) [4,17,18] and the use theoretical models of failure criteria [4,19,20]. A number of authors have conducted research along models of failure criteria, but no studies were found that investigated failure criteria in polymer composites using hybrid fabrics. As such, a large number of investigations have involved experimental and numerical analysis in order to quantify stress concentration in composites using failure theories such as Point Stress Criterion (**PSC**) and Average Stress Criterion (**ASC**) [21–23]. Carbon fiber composites exhibit excellent mechanical and thermal properties. However, limited production and high costs hinder their use, limiting their application to such areas as luxury cars, the aerospace industry [9] and sports equipment for professional athletes. Hybridization with other fibers, such as glass and aramid, may widen their use, since they exhibit a good cost/benefit ratio for engineering, such as applying a carbon/glass hybrid polymer composite with an epoxy matrix in the construction of wind turbine rotor blades [11].

The novelty of the study is the use of hybrid fabrics to optimize the cost/mechanical performance relationship in structural applications by examining the influence of anisotropy and geometric discontinuity on two hybrid fabric-reinforced polymer composites, one with carbon (T300)/E-glass fibers and the other using carbon (T300)/aramid (Twaron) fibers and the epoxy vinyl ester thermosetting resin (Derakane Momentum™ 411-350) was used as matrix for both laminates. Normally one of the fibers in a hybrid composite is a costly, high modulus variety, such as boron or carbon, while the other is generally a low elastic modulus fiber, such as E-glass and

* Corresponding author.
E-mail address: ana.batista@ufersa.edu.br (A.C.M.C. Batista).

http://dx.doi.org/10.1016/j.compositesb.2017.05.066
1359-8368/

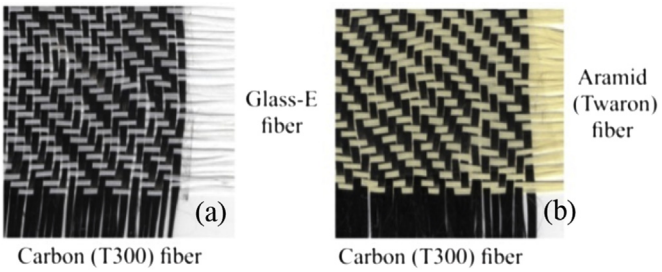

Fig. 1. a) Hybrid fabric – carbon/glass fibers; (b) Hybrid fabric – carbon/aramid fibers.

Kevlar [10]. The presence of a central hole was analyzed in conjunction with anisotropy in the direction of load application (0°, 90° and 45°), in test specimens with no hole and those with a central hole. It is important to underscore the influence of anisotropy associated with the presence of a central hole, making the investigation more complex. Finally, analyses of final fracture characteristics at macroscopic levels were performed in order to understand the effects of the holes and anisotropy on composite laminates.

2. Materials and methods

2.1. Composite laminates

The composite laminates studied exhibit ten layers of hybrid fabric as reinforcement and use epoxy vinyl ester thermosetting resin as matrix. They are commercially designed by DERAKANE MOMENTUM™ 411-350. The agent of the catalytic system (cured at ambient temperature) was 1% MEKP (methyl ethyl ketone peroxide) and 0.05% of 6% cobalt naphthenate, composites suggested in the technical bulletin for resin at a temperature of 30 °C. The manufacturing (industrial) process used was hand lay-up.

Twill weaving was used in both hybrid fabrics (see Fig. 1). The hybrid fabric with carbon/glass fibers ((Fig. 1(a)) was used to manufacture the Carbon/Glass Composite Laminate (denominated **CGL**), while the carbon/aramid fiber hybrid fabric ((Fig. 1(b)) was used to manufacture the Carbon/Aramid Composite Laminate (denominated **CAL**). **CGL** and **CAL** laminate thicknesses were approximately 2.55 ± 0.08 mm and 3.83 ± 0.24 mm, respectively.

In light of the different reinforcement characteristics, the test specimens were cut with two different types of cutting disc: an IRWIN Ø4 - 3/8″ x 3/4” (110 mm × 20 mm) segmented diamond cutting blade and BOSCH Ø4 3/8” (110 mm × 20 mm) Optiline Wood circular saw blade, for the **CGL** and **CAL** laminates, respectively. After cutting, the specimens were sanded and polished to obtain the standard finish and dimensions.

A 6 mm milling cutter was used to machine the central hole. The milling tool is not generally used to make holes, but since aramid and Kevlar fiber-reinforced composites are difficult to machine [24], it was used to achieve a better finish. No delaminations or microcracks were observed in macroscopic and microscopic analyses after drilling.

To analyze the results, a specific nomenclature for the specimens was needed, considering each type of fiber and the load application directions (0°, 90° and ±45°) for both laminates. Samples with no central hole are specified as in the original condition. Tables 1 and 2 show the nomenclature adopted in this research.

2.2. Density and calcination testing

To determine the density of the laminates, we used test method A for testing solid plastics in water (specimens 1–50 g) according to ASTM D 792 [25] standard. Five test specimens were prepared for each type of composite laminate (25 × 25 mm) and the results averaged. To that end, we used a Shimadzu AUY 220 digital weighing machine with 0.1 mg resolution and maximum capacity of 220 g.

The calcination test was applied to determine the volume fractions of reinforcement, resin and voids. After the density was determined, the resin was calcined, the samples were placed in a ceramic crucible, heated in the muffle for 4 h at 400 °C - 450 °C, and the weight loss was related to the fabric. The percentage of each fiber, for each fabric, was calculated applying the titration test to the yarn. The equation in the D3171 [26] standard was used to determine the volumetric percentage of each constituent. The density values of 1.14 g/cm^3, 1.76 g/cm^3, 2.54 g/cm^3 and 1.44 g/cm^3 for resin, carbon fiber T300, glass fiber/E and aramid fiber (Twaron), respectively, were used to calculate volumetric percentages.

Table 1
Specimens definition to **CGL**.

Specimen's	Definition
$\mathbf{CG^{C}}$	Original condition with load applied in the direction of the carbon fibers.
$\mathbf{CG^{G}}$	Original condition with load applied in the direction of the glass fibers.
$\mathbf{CG^{\pm 45^{\circ}}}$	Original condition with load applied in the direction of both fibers at 45°.
$\mathbf{CG^{C}_{\varnothing 6}}$	Central hole condition with load applied in the direction of the carbon fibers.
$\mathbf{CG^{G}_{\varnothing 6}}$	Central hole condition with load applied in the direction of the glass fibers.
$\mathbf{CG^{\pm 45^{\circ}}_{\varnothing 6}}$	Central hole condition with load applied in the direction of both fibers at 45°.

Table 2
Specimens definition to **CAL**.

Specimen's	Definition
$\mathbf{CA^{C}}$	Original condition with load applied in the direction of the carbon fibers.
$\mathbf{CA^{A}}$	Original condition with load applied in the direction of the aramid fibers.
$\mathbf{CA^{\pm 45^{\circ}}}$	Original condition with load applied in the direction of both fibers at 45°.
$\mathbf{CA^{C}_{\varnothing 6}}$	Central hole condition with load applied in the direction of the carbon fibers.
$\mathbf{CA^{A}_{\varnothing 6}}$	Central hole condition with load applied in the direction of the aramid fibers.
$\mathbf{CA^{\pm 45^{\circ}}_{\varnothing 6}}$	Central hole condition with load applied in the direction of both fibers at 45°.

2.3. Uniaxial tensile test

Uniaxial tensile tests in test specimens without and with a hole were conducted, using ASTM D3039 [27] and D5766/D5766M [28] standards, respectively. A SHIMADZU AGX universal testing machine, with maximum capacity of 300 kN, was used to conduct the test. The tests were performed at a displacement velocity of 2.0 mm/min at ambient temperature. The dimensions for the specimens without a hole were 250 mm × 25 mm [27] and those with a hole 250 mm × 36 mm (length x width) [28], with a tolerance of 1%, according to their respective technical standard. The gauge length of all test specimens was 127 mm. The standard [27] specifies that is necessary at least five specimens per test condition. The strains were measured by strain gage of the own universal testing machine.

2.4. Fracture analysis

The macroscopic fracture was characterized and based on ASTM standards D3039 [27] and D5766 [28], which describe and characterize all types of valid fractures. Images were obtained using an EPSON L355 multifunctional printer scanning system.

2.5. Residual properties: *PSC* and *ASC* failure theories

The influence of reduced tensile strength and Young's modulus on composite laminates, due to the presence of geometric discontinuity, was studied using the Residual Strength (RS) and Residual Modulus (RM) of composite laminates [4,27–29], according to the following equations:

$$RS = \frac{\sigma_{Notched}}{\sigma_{Unnotched}} \tag{1}$$

$$RM = \frac{E_{Notched}}{E_{Unnotched}} \tag{2}$$

where: $\sigma_{Notched}$ is defined as the ultimate tensile strength of test specimens with a hole (calculated in the area of largest cross-section section, according to ASTM standard D 5766 [28]); $\sigma_{Unnotched}$ corresponds to the ultimate tensile strength of test specimens without a hole; $E_{Notched}$ and $E_{Unnotched}$ correspond to Young's longitudinal modulus (measured in the direction of load application) of test specimens with and without a hole, respectively.

Over the years, some criteria have attempted to predict the Residual Strength of composites in the presence of a circular hole, using the Point-Stress Criterion (**PSC**) and Average-Stress Criterion (**ASC**) failure theories. The challenge in this study is the viability of using these failure theories in fabric-reinforced hybrid composite laminates.

According to Tan [23]: these two stress criteria use the stress field to predict the notched strength without resorting to the classical concepts of linear elastic fracture mechanics and these criteria are based on the observation of the stress fields around a hole with different sizes. The two stress criteria (**PSC** and **ASC**) are demonstrated below.

The **PSC** assumes that failure will occur when stress (σ_N) at a certain small fixed distance d_0 before the hole boundary first reaches the tensile strength σ_f of the material (or the tensile strength of the specimen without a hole, σ_{UN}) [30]. According to Nuismer and Whitney [31] and Tan [23], this residual strength can be expressed as:

$$RS_{PSC} = \frac{\sigma_N}{\sigma_{UN}} = \frac{2}{2 + \xi_1^2 + 3\xi_1^4 - \left(K_{T,o,p,u}^{\infty,1} - 3\right)\left(5\xi_1^6 - 7\xi_1^8\right)} \tag{3}$$

where:

$$\xi_1 = \frac{R}{R + d_0} \tag{4}$$

R is defined as the hole radius, $K_{T,o,p,u}^{\infty,1}$ is the stress concentration factor [32] and d_0 is some distance, away from the opening that the stress is equal to or greater of the unnotched laminate.

The **ASC** assumes that failure will occur when the average stress value (σ_N) over some small fixed distance a_0 before the hole boundary first reaches tensile strength σ_f of the material (or the tensile strength of the plate without a hole, σ_{UN}) [30]. According to Nuismer and Whitney [31] and Tan [23], this residual strength can be expressed as:

$$RS_{ASC} = \frac{\sigma_N}{\sigma_{UN}} = \frac{2(1 - \xi_2)}{2 - \xi_2^2 - \xi_2^4 + \left(K_{T,o,p,u}^{\infty,1} - 3\right)\left(\xi_2^6 - \xi_2^8\right)} \tag{5}$$

where:

$$\xi_2 = \frac{R}{R + a_0} \tag{6}$$

R is also defined as the hole radius, $K_{T,o,p,u}^{\infty,1}$ is the stress concentration factor [32] and a_0 is some distance away from the opening that the average stress is equal to or greater of the unnotched laminate.

It is worth pointing out that for materials considered isotropic or quasi-isotropic, the value of K in both criteria, is 3.0 (three). The values of the characteristic distances d_0 and a_0 are generally determined by the averages of the curves of experimental data found through tensile testing of several specimens with different hole sizes, and in some literature data [31] d_0 is equal to 1.0 mm and a_0 to 3.75 mm. The models also show that the values of the distances d_0 and a_0 depend on the fiber/matrix system and the configuration of the laminate.

3. Results and discussion

3.1. Density and calcination testing

The results for the volumetric densities of the laminates and the percentages of their volumetric fractions are shown in Table 3. Although the carbon fiber percentage differs in **CGL** and **CAL**, titration of carbon fiber roving is identical for both fabrics. Table 3 shows the low void percentage (less than 1%); this percentage is higher in other hybrid composite laminates with similar fibers, reaching 10% [12]. This was possible due to the use of a vacuum pump to remove air bubbles from the resin before starting lamination.

3.2. Study of anisotropy – *CGL* – original condition

Fig. 2 shows the mechanical behaviors obtained in uniaxial tensile tests in stress/strain diagrams for **CGL** (in the original condition). Also reported are the respective means and standard deviations of tensile strength (σ), Young's modulus (E) and Elongation (ε) for 0°, 90° and 45°, respectively for specimens $\mathbf{CG^C}$, $\mathbf{CG^G}$ and $\mathbf{CG^{\pm 45^\circ}}$.

Fig. 2 (a) shows that the stress/strain profile exhibited by specimens $\mathbf{CG^C}$ is uncommon for composite materials in general,

Table 3
Volumetric density and fractions of **CGL** and **CAL**.

Laminates	Volumetric density (g/cm^3)	Glass fiber (%)	Carbon fiber (%)	Kevlar fiber (%)	Matrix (%)	Voids (%)
CGL	1.48 ± 0.01	14.98 ± 0.53	21.62 ± 0.77	–	62.42 ± 1.27	0.98 ± 0.02
CAL	1.29 ± 0.01	–	15.73 ± 0.66	16.51 ± 0.69	67.31 ± 1.3	0.44 ± 0.11

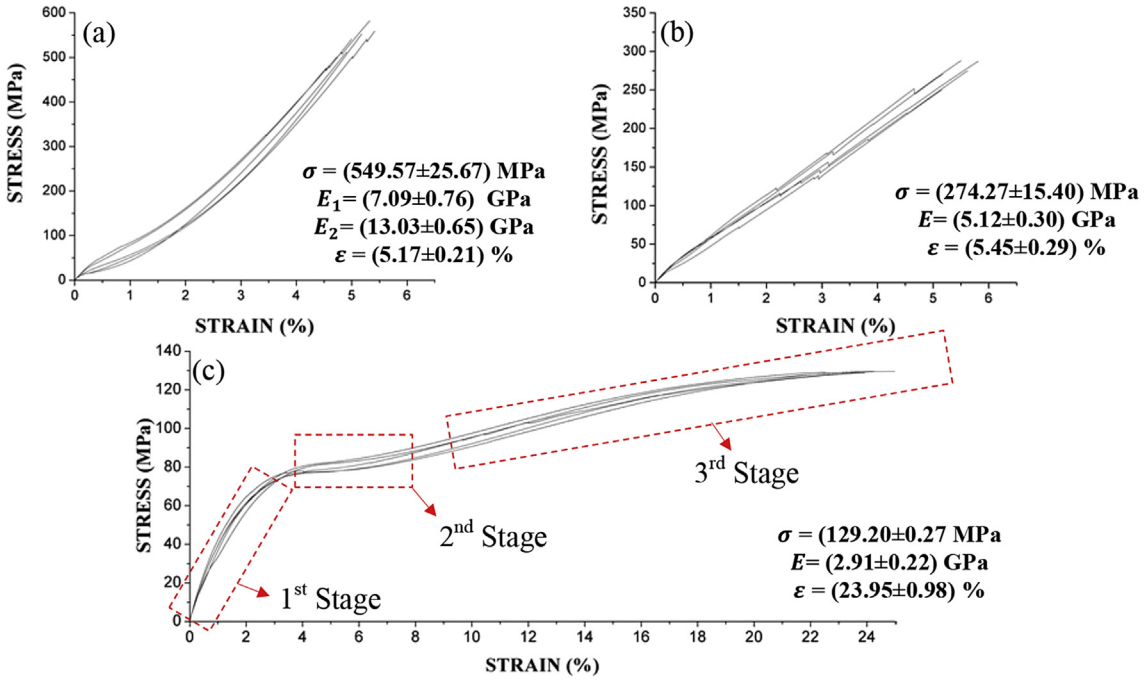

Fig. 2. Stress/strain diagram for: (a) **CG^C**; (b) **CG^G**; (c) **CG$^{\pm 45^\circ}$**.

that is, a nonlinear profile, characterized by an increase in Young's modulus (measured in the direction of the applied load) during loading. Given this atypical behavior, a more accurate analysis of Young's modulus is needed. To that end, bilinear behavior is initially proposed for this profile (based on the mean **CG^C** curve) (see Fig. 3 (a)), in order to confirm that the material exhibits two Young's modulus during loading. The Fig. 3 (b) shows the same behavior for **CG^C** in the load x displacement diagram obtained by the mean of the valid test curves.

In this respect, the stress intensity at which the modulus initially changes was determined, approximately 150 MPa (around 30% tensile strength, that is, the fracture stress of specimens). The first modulus (defined as the initial Young's modulus) is calculated for a stress range between 0 and 150 MPa and the second modulus (defined as the final Young's modulus) for a stress range between 150 MPa and approximately 510 MPa, related to the onset of the fracture process.

Fig. 3 (a) also shows that the slope of the final Young's modulus is much higher than that of the initial modulus, characterizing an increase and representing a predominant behavior (around 70% of the test until final rupture).

An important characteristic in the tensile behavior of this

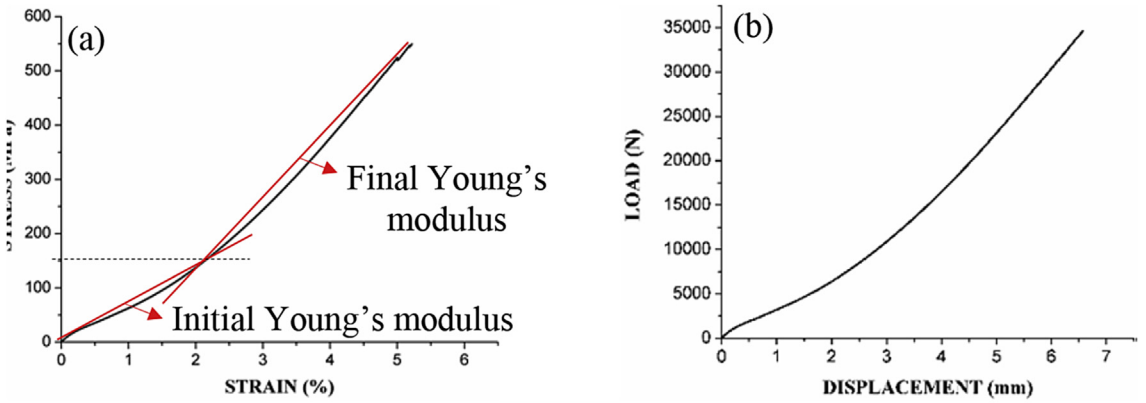

Fig. 3. (a) Stress/strain diagram for **CG^C** with the Young's modulus; (b) Load x displacement diagram.

laminate in the direction of the carbon fibers is the high load at the onset of damage, which is close to the load responsible for the final fracture of the laminate. The change recorded in Young's modulus is not due to the initial process of the damage, as reported in Ref. [4] for notched fiber-reinforced plastic. For other hybrid composite configurations (primarily with hybridization in laminate layers), studies such as those by Zang et al. [9] and Guermazi et al. [14], show no changes in the respective Young's moduli until final fracture of the specimens. In the study by Pandya et al. [10], the graph showed a slight change in behavior near stress rupture, but in the sense of decreasing the modulus.

It is important to underscore that in the aforementioned studies, the change in Young's modulus was always a loss of its intensity, caused by the onset of damage, contrasting with the behavior recorded in **CG^{C}**. This reflects a possible adaptation of the widely varying Young's modulus of the fibers contained in the hybrid fabric, that is, E-glass fibers with a modulus of 70 GPa [33] and carbon fibers (T300) with 230 GPa [34]. Even though these are isolated fiber values not affected by fabric or resin weaving (fiber/matrix interface), their properties are not lost in the conception process of the composite material, but rather adapt.

Unlike **CG^{C}**, the mechanical behavior of **CG^{G}** (Fig. 2 (b)) exhibits a linear profile between stress and strain until final fracture. Successive losses and immediate recovery of load support capacity was also observed. This behavior may be related to the fact that the glass fibers fractured before carbon fibers, partly due to the significant difference in tensile strength values between glass (2200 MPa) [33] and carbon fibers (3100 MPa) [34].

The tensile behavior obtained for **CG$^{\pm 45^{\circ}}$** is represented in Fig. 2(c), with no linearity observed between stress and strain during the test due to the considerable influence of anisotropy, that is, fiber direction in relation to the direction of the applied load. It is important to underscore the presence of shearing in the response of specimens. For better understanding, the profile of the curves is divided into three stages:

- **1st stage:** linear behavior, predominantly tensile behavior of the material and segment used to determine Young's modulus;
- **2nd stage:** onset of shearing, defined as the transition stage;
- **3rd stage:** predominantly shear behavior under uniaxial tensile testing. Continued load support, with high strain capacity.

The test demonstrated that strain capacity was so intense for **CG$^{\pm 45^{\circ}}$** that the specimen constrict in the transverse section before final rupture, a phenomenon explained by the characteristic of a mechanical fracture. In this type of fabric (hybridization jointly with the type of weaving), the mechanical response of the material is strongly linked to the damage process.

Similar behavior, with high strain capacity, was also found by Bergmann et al. [35], where the author shows tensile behavior with fibers oriented at ±45° for several composite laminates involving different types of fibers (carbon, glass, aramid, Vectran®, and Dyneema®); fabrics (bidirectional, twill weaving, sateen and braid); and resins (2 types of epoxy resin and PEEK thermosplastic resin) using 8 layers. The same author reported similar behavior for several laminates oriented at ±45° under uniaxial tensile loading, and that ASTM standard D3518/D3518M [36] prevented high strain when the test specimen exhibits pure shearing (orientation at ±45°).

Tinô et al. [18] demonstrated distinct behavior for a bidirectional fiber-reinforced composite laminate (balanced) of E-glass fibers oriented at ±45°, submitted to uniaxial tensile loading, finding no strain in the shear stage (5.51% strain until total fracture), or specimen constriction.

3.3. Characteristic of the mechanical fracture - *CGL* – original condition

The **CG^{C}** did not exhibit initial microcracking and the onset of damage load occurred close to the stress of the final fracture, characterizing it as a fragile or brittle material. The macroscopic fracture is depicted in Fig. 4(a), showing that the fracture is always near the tabs, and is classified at **LAT** (Lateral - At grip/tab Top) [27].

The **CG^{G}** fracture (Fig. 4(b)) shows that none of the test specimens exhibited fiber tearing, characteristic damage in glass fiber-reinforced polymer composites (in the direction of the tensile load) and also reported by Tinô et al. [4] and Batista et al. [12]. Fig. 4(b) demonstrates that the test specimens exhibited two successive fracture regions (not covered by ASTM standard D3039 [27]), but the specimen broke in only one of these fracture regions. At any rate, in some specimens, the total rupture mode can be classified as **LGM** (Lateral Gage Middle) [27] and in others as **LAT** (Lateral -At grip/tab Top) [27].

Tabs were not used for **CG$^{\pm 45^{\circ}}$** (Fig. 4(c)), since they are normally not required by ASTM standards D3518 [36]. It is important to underscore that the fracture mode of these specimens is not covered by ASTM standard D3039 [27], due to the constriction process. At the onset of constriction in the tensile test, fiber/matrix debonding was detected in the glass fibers.

Bergmann et al. [35] explains that the effect of shearing is a matrix-dominated failure mode, initiated by microcracking and matrix failure, allowing fiber rovings to rotate in the direction of the load. Fiber reorientation results in high strain until failure, which is necessary for tensile energy absorption. The increase in energy absorption capacity is accompanied by a reduction in stiffness and strength in this direction (±45°).

3.4. Study of anisotropy – *CAL* – original condition

Fig. 5 shows the mechanical behavior with the respective mean values and standard deviation of tensile strength (σ), Young's modulus (E) and Elongation (ε) of **CAL** specimens without a hole for directions 0°, 90° and 45°, for **CA^{C}**, **CA^{A}** and **CA$^{\pm 45^{\circ}}$**, respectively.

Fig. 5 (a) shows that the **CA^{C}** specimens displayed linear behavior between stress and strain until final fracture. This characteristic behavior is common in thermoset resin-based polymer composites. The **CA^{A}** also displayed the same linear profile between stress and strain until final fracture, as depicted in Fig. 5 (b).

The tensile characterization of **CA$^{\pm 45^{\circ}}$**, using the stress/strain graph in Fig. 5 (c), shows a profile with distinct characteristics, that is, with the specimens' initial tensile response, followed by the shear response. For better understanding, the graph is divided into two stages:

- **1st stage:** Linear behavior (predominantly tensile behavior); and
- **2nd stage:** Shear behavior, high strain, with no load support.

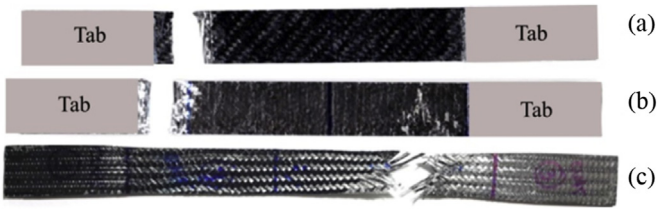

Fig. 4. Macroscopic fracture: (a) **CG^{C}**; (b) **CG^{G}**; (c) **CG$^{\pm 45^{\circ}}$**.

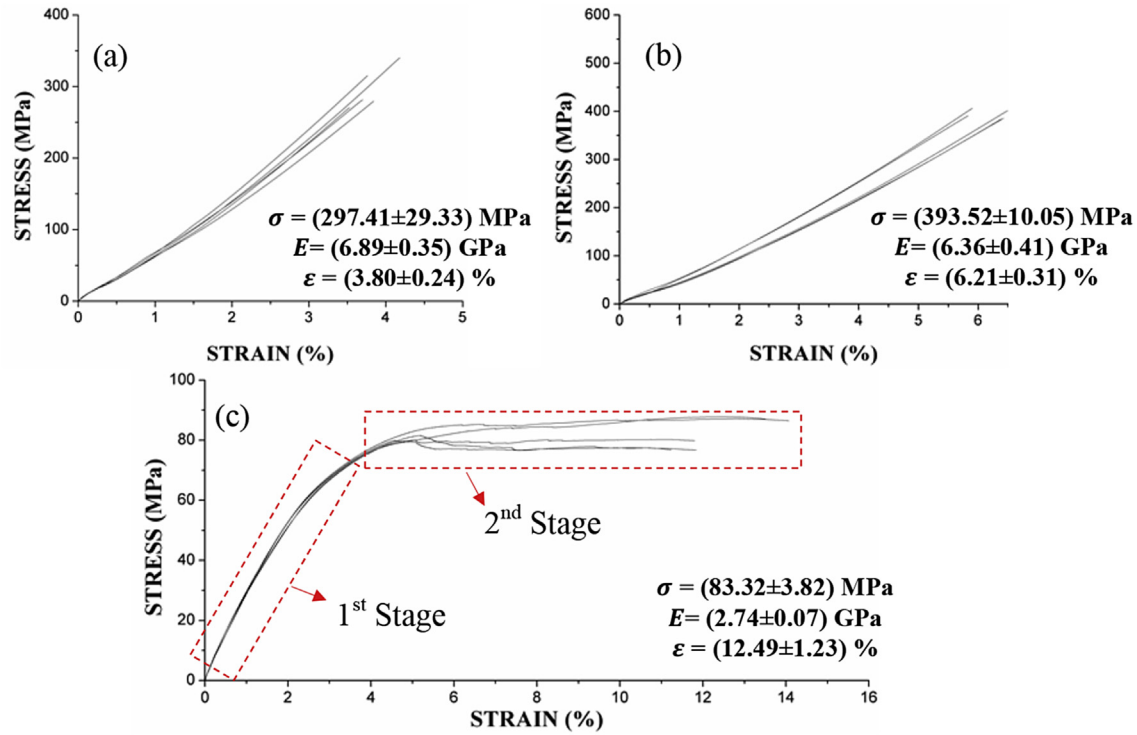

Fig. 5. Stress/strain diagram for: (a) $\mathbf{CA^{C}}$; (b) $\mathbf{CA^{A}}$; (c) $\mathbf{CA^{\pm 45^{\circ}}}$.

The mean values and standard deviation values of $\mathbf{CA^{\pm 45^{\circ}}}$ indicate that tensile strength and Young's modulus displayed low standard deviation values (less than 5% and 2.6% of the mean value, respectively), while the rupture strain showed high standard deviation of around 10% of the mean value. This high variation in strain values may be explained by the fracture process.

$\mathbf{CA^{A}}$ displayed higher tensile strength than that of $\mathbf{CA^{\pm 45^{\circ}}}$ when compared to $\mathbf{CA^{C}}$. It is important to underscore that when the direction of the applied load coincides with that of carbon fibers, greater tensile strength is normally expected. However, the T300 carbon fibers (of Pitch isotropic origin) used in the hybrid fabric exhibit lower tensile strength than that of other carbon fibers [33]. Depending on the grammage of the fabric and titration of the roving, it is possible to obtain greater strength when the load direction coincides with the direction of aramid fibers, when compared to the coincidence of the load applied in the direction of carbon fibers.

3.5. Characteristics of mechanical fractures – CAL – original condition

Fracture analysis at the macroscopic level demonstrates that the fracture mode in $\mathbf{CA^{C}}$ (Fig. 6 (a)) is **LGM** (Lateral Gage Middle) [27] and that cracks are concentrated in the final fracture region.

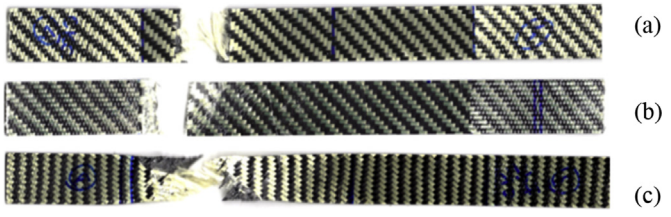

Fig. 6. Macroscopic fracture: (a) $\mathbf{CA^{C}}$; (b) $\mathbf{CA^{A}}$; (c) $\mathbf{CA^{\pm 45^{\circ}}}$.

The macroscopic characteristic of the fracture that occurred in $\mathbf{CA^{A}}$ is also **LGM** (Lateral Gage Middle) [27]. However, the specimen also exhibited an intense microcracking region in the matrix and aramid fiber tearing in the final fracture region, as can be seen in the $\mathbf{CA^{A}}$ fracture in Fig. 6 (b). The cracks are transverse to the direction of loading and found along the entire useful length of the specimens.

Fig. 6 (c) shows the macroscopic analysis of the fracture in $\mathbf{CA^{\pm 45^{\circ}}}$ and that the fracture mode exhibits the same constriction that occurred during the shear stage, but at lower intensity. This explains the different strain intensities in the fracture, that is, around 25% and 14% for $\mathbf{CG^{\pm 45^{\circ}}}$ and $\mathbf{CA^{\pm 45^{\circ}}}$, respectively.

As previously explained and according to Bergmann et al. [35], fiber reorientation results in high strain until fracture and, given that the fiber roving's rotate in the loading direction, the matrix-dominated failure mechanism is triggered by microcracks and fiber/matrix debonding.

3.6. Study of anisotropy – **CGL** – central hole condition

The mechanical behavior with respective mean values and standard deviations of tensile strength (σ), Young's modulus (E) and Elongation (ε) of **CGL** specimens with a hole at 0°, 90° and 45° for $\mathbf{CG^{C}_{\varnothing 6}}$, $\mathbf{CG^{G}_{\varnothing 6}}$ and $\mathbf{CG^{\pm 45^{\circ}}_{\varnothing 6}}$, respectively, are shown in Fig. 7.

Fig. 7 (a) shows a nonlinear profile between stress and strain in $\mathbf{CG^{C}_{\varnothing 6}}$, characterized by the change in Young's modulus during loading, a behavior similar to that obtained in $\mathbf{CG^{C}}$ (original condition). Therefore, $\mathbf{CG^{C}_{\varnothing 6}}$ also displayed two moduli, that is, bilinear behavior, as observed in Fig. 8. The stress that occurs in this transition is around 55 MPa, approximately 18% of tensile strength.

As such, the initial Young's modulus (E_1) is calculated for the range between 0 and 55 MPa and the final Young's modulus (E_2) for a stress range between 55 MPa and 275 MPa, the stress related to the onset of the fracture. The E_1 and E_2 values depicted in Fig. 7 (a)

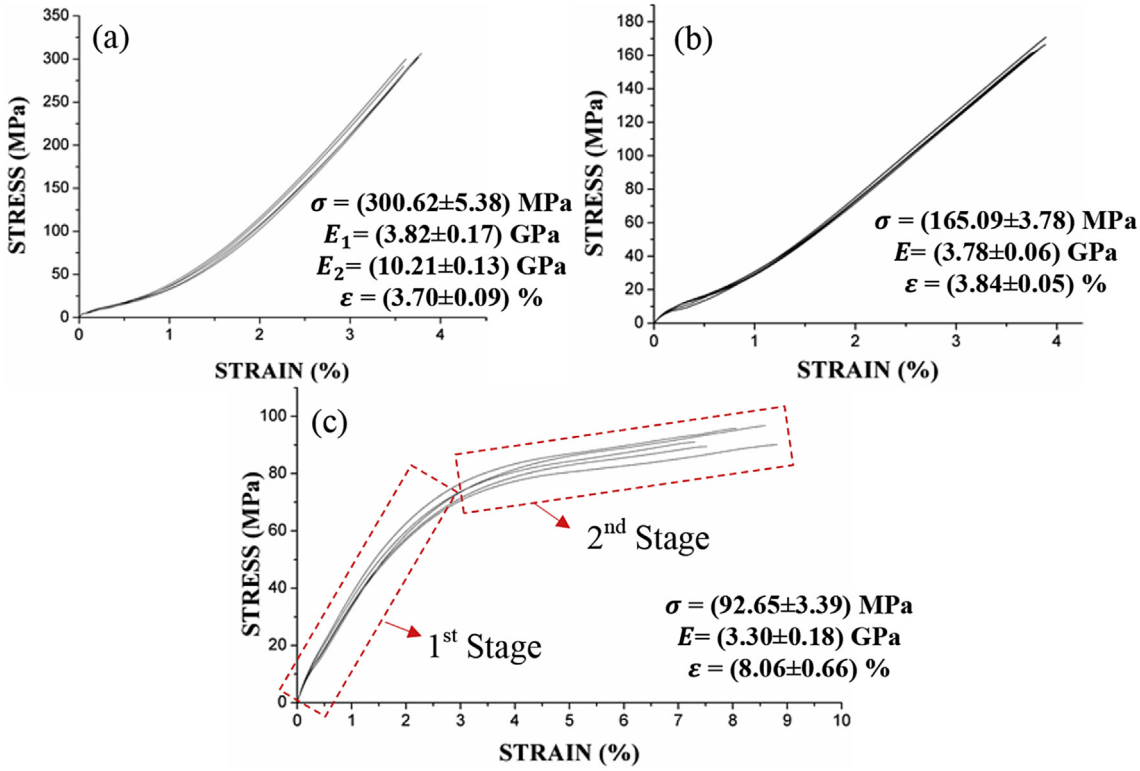

Fig. 7. Stress/strain diagram for: (a) $\mathbf{CG}^{\mathbf{C}}_{\varnothing 6}$; (b) $\mathbf{CG}^{\mathbf{G}}_{\varnothing 6}$; (c) $\mathbf{CG}^{\pm 45^{\circ}}_{\varnothing 6}$.

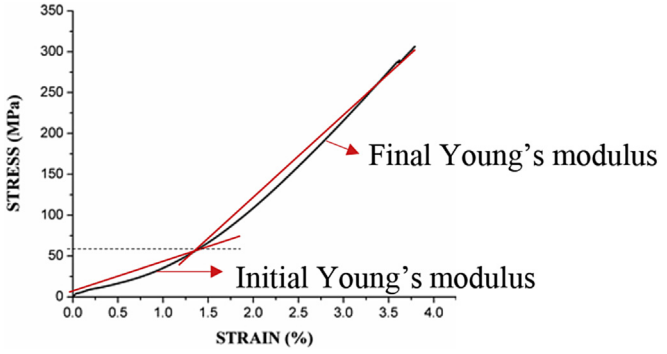

Fig. 8. Stress/strain diagram for $\mathbf{CG}^{\mathbf{C}}_{\varnothing 6}$ with the Young's modulus.

demonstrate that the slope of the final Young's modulus is much higher to that of the initial modulus (around 2.7 fold), representing predominant behavior (around 82% of the test until final rupture).

It is important to underscore that, like $\mathbf{CG}^{\mathbf{C}}$, $\mathbf{CG}^{\mathbf{C}}_{\varnothing 6}$ also exhibits a high load at the onset of damage, which is close to that responsible for the final fracture, as well as bilinear behavior, possibly due to the significant difference in Young's modulus between glass and carbon fiber.

$\mathbf{CG}^{\mathbf{G}}_{\varnothing 6}$ displayed a profile between stress and strain that can be considered linear (Fig. 7 (b)), since the slight loss of linearity initially observed is attributed to the adjustment of the specimens in the clamps of the test machine. This did not occur for $\mathbf{CG}^{\mathbf{G}}$, which exhibited linear stress/strain behavior.

Furthermore, $\mathbf{CG}^{\mathbf{G}}_{\varnothing 6}$ also showed no successive load losses and recoveries as occured in $\mathbf{CG}^{\mathbf{G}}$. This may be explained by the characterization of the fracture, highly concentrated in the hole region and described in the next topic.

$\mathbf{CG}^{\pm 45^{\circ}}_{\varnothing 6}$ showed similar mechanical behavior, characteristic of specimens with fibers oriented at 45° and illustrated in Fig. 7 (c). They exhibited linearity between stress and strain in the initial stage of the test, reflecting their tensile strength. Next, the characteristic shear behavior can be observed with the presence of intense strain and little load support capacity. For a better understanding, the curve profile is divided into two stages:

- **1st Stage:** Linear behavior, predominantly tensile behavior in the material and the segment used to determine Young's modulus;
- **2nd Stage:** Predominantly shear behavior under uniaxial tensile testing. Continuation of part of the load support, with high strain.

The presence of a hole changed the profile of the stress/strain graph, since $\mathbf{CG}^{\pm 45^{\circ}}$ exhibited three well-defined stages, whereas $\mathbf{CG}^{\pm 45^{\circ}}_{\varnothing 6}$ had only two, not displaying the second stage (onset of shearing, defined as the transition stage).

Other studies involving the effect of anisotropy with a central hole using carbon fibers and glass fibers as reinforced can be found in papers such as Toubal [37] and Tinô 2011 [18], respectively.

*3.7. Characteristic of the mechanical fracture – **CGL** – central hole condition*

Macroscopic analysis of $\mathbf{CG}^{\mathbf{C}}_{\varnothing 6}$, $\mathbf{CG}^{\mathbf{G}}_{\varnothing 6}$ and $\mathbf{CG}^{\pm 45^{\circ}}_{\varnothing 6}$ fractures is shown in Fig. 9. For $\mathbf{CG}^{\mathbf{C}}_{\varnothing 6}$, Fig. 9 (a), the fracture occurred at the hole and can be characterized as **LGM** [28] (Laminate tensile failure laterally across the center of the hole. Cracks and delaminations may be present). However, no cracks or delaminations were observed, and damage started near the final fracture.

The $\mathbf{CG}^{\mathbf{G}}_{\varnothing 6}$ fracture in Fig. 9 (b) shows glass fiber/matrix

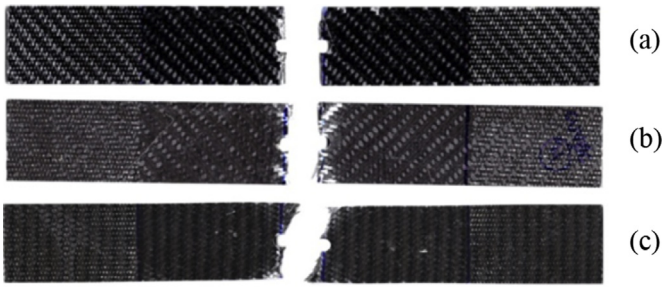

Fig. 9. Macroscopic fracture: (a) $\mathbf{CG}^{\mathbf{C}}_{\varnothing 6}$; (b) $\mathbf{CG}^{\mathbf{G}}_{\varnothing 6}$; (c) $\mathbf{CG}^{\pm 45^{\circ}}_{\varnothing 6}$.

debonding in the fracture region. The fracture is characterized as **LGM** [28] (Laminate tensile failure laterally across the center of the hole. Cracks and delaminations may be present), despite the non-occurrence of cracks and delaminations. In the $\mathbf{CG}^{\mathbf{G}}_{\varnothing 6}$ fracture, damage is located in the region of the hole, because geometric discontinuity acts as a concentrator of stress, explaining why the successive load losses or recoveries observed in $\mathbf{CG}^{\mathbf{G}}$ did not occur.

The macroscopic fracture (Fig. 9 (c)) of $\mathbf{CG}^{\pm 45^{\circ}}_{\varnothing 6}$ is the **AGM** [28] type (laminate generally stress-related failure at the hole, but remnants of angle plies cross the lateral centerline of the hole. Cracks and delaminations may be present), characterized by a fracture concentrated in the region of the hole, with no cracks or fiber/matrix debonding. The fracture was concentrated in the region of the hole and not along the entire length of the test specimen, as occurred in $\mathbf{CG}^{\pm 45^{\circ}}$. Intense strain was noted during the test, concentrated in the region near the hole, making it elliptic. The hole likely acted as a stress concentrator and initiated shear stress in the region around it, allowing fibers to rotate toward the loading direction. No test specimens were found with fibers oriented at ±45° to the hole.

3.8. Study of anisotropy — CAL — central hole condition

Fig. 10 illustrates the mechanical behavior with the respective mean values and standard deviations for the tensile strength (σ), Young's modulus (E) and Elongation (ε) of **CAL** specimens with the presence of a hole and at directions 0°, 90° and 45°, for $\mathbf{CA}^{\mathbf{C}}_{\varnothing 6}$, $\mathbf{CA}^{\mathbf{A}}_{\varnothing 6}$ and $\mathbf{CA}^{\pm 45^{\circ}}_{\varnothing 6}$, respectively.

The stress/strain profile of $\mathbf{CA}^{\mathbf{C}}_{\varnothing 6}$ ((Fig. 10 (a)) displayed linear elastic behavior until final fracture, a characteristic of thermoset resin-based polymer composites. It is important to underscore that the presence of a hole did not change this profile for **CAL**. Fig. 10 (b) demonstrates that the mechanical characterization of $\mathbf{CA}^{\mathbf{A}}_{\varnothing 6}$ can be considered linear elastic and uniform behavior until final fracture. Similar behavior was obtained for $\mathbf{CA}^{\mathbf{C}}_{\varnothing 6}$, indicating that the presence of a hole, in terms of the stress/strain profile, maintains fiber orientation in the direction of the carbon and aramid fibers.

The mechanical behavior characteristic of $\mathbf{CA}^{\pm 45^{\circ}}_{\varnothing 6}$ is presented in Fig. 10 (c), where the characteristic stress/strain curve shows nonlinear behavior, typical of this type of loading with fibers oriented at ±45° in relation to the application of the load. The same analysis conducted for the earlier cases is applied here, that is, behavior can be divided into two stages:

- **1st Stage:** Linear behavior between stress and strain, considered the tensile response of the test specimens;
- **2nd Stage:** Characteristic shear behavior, that is, high strain with a small amount of load support.

The behavior of $\mathbf{CA}^{\pm 45^{\circ}}_{\varnothing 6}$ is different from that of $\mathbf{CA}^{\pm 45^{\circ}}$, given that these specimens do not exhibit any load support capacity at the onset of the 2nd stage. In this respect, the only factor of influence would be the presence of a hole.

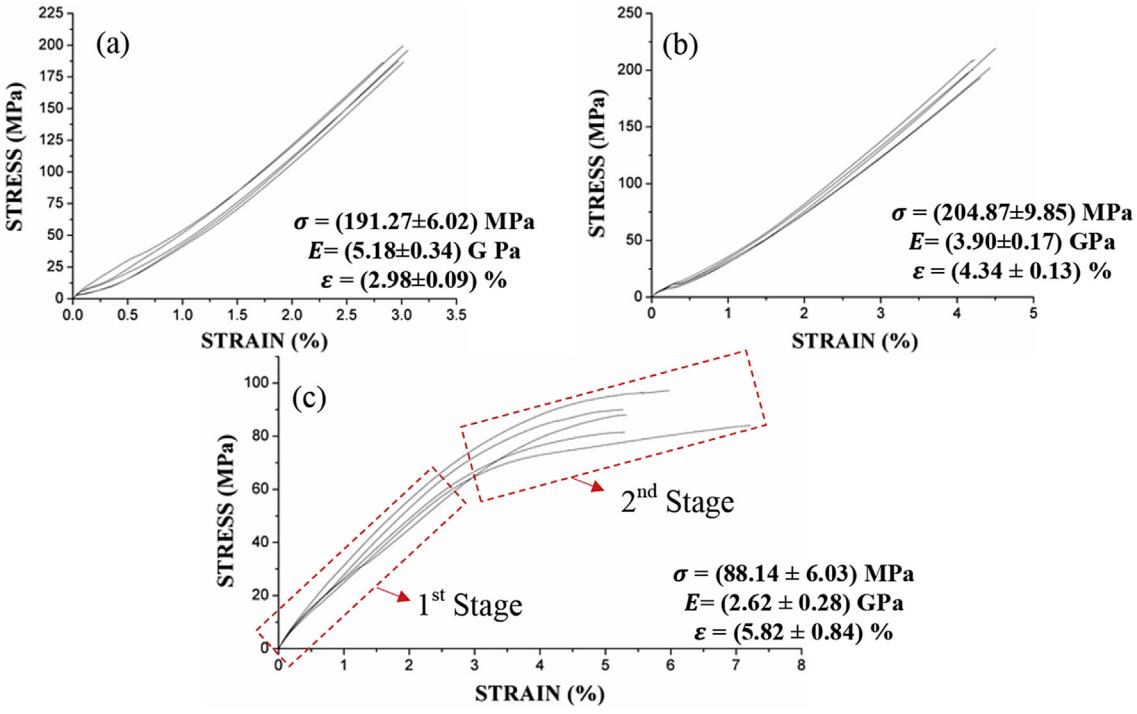

Fig. 10. Stress/strain diagram for: (a) $\mathbf{CA}^{\mathbf{C}}_{\varnothing 6}$; (b) $\mathbf{CA}^{\mathbf{A}}_{\varnothing 6}$ e $\mathbf{CA}^{\pm 45^{\circ}}_{\varnothing 6}$.

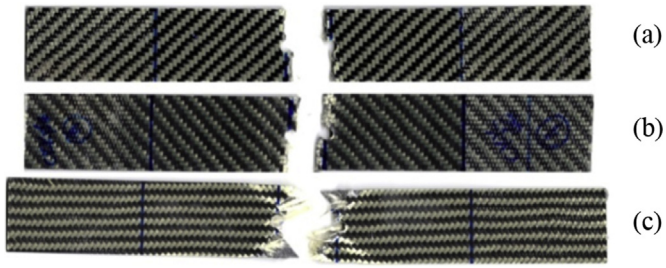

Fig. 11. Macroscopic fracture: (a) $\mathbf{CA}^{\mathbf{C}}_{\varnothing 6}$; (b) $\mathbf{CA}^{\mathbf{A}}_{\varnothing 6}$ e, (c) $\mathbf{CA}^{\pm 45^{\circ}}_{\varnothing 6}$.

3.9. Characteristic of the mechanical fracture – CAL – central hole condition

The characteristic of the macroscopic fracture in $\mathbf{CA}^{\mathbf{C}}_{\varnothing 6}$, $\mathbf{CA}^{\mathbf{A}}_{\varnothing 6}$ and $\mathbf{CA}^{\pm 45^{\circ}}_{\varnothing 6}$ is shown in Fig. 11. The fracture in $\mathbf{CA}^{\mathbf{C}}_{\varnothing 6}$ is presented in Fig. 11 (a), showing that the fracture occurs around the hole, and is characterized as **LGM** [28] (laminate tensile failure laterally across the center of the hole. Cracks and delaminations may be present). Two cracking regions were found near the final fracture and no aramid fiber tearing was observed.

Fig. 11 (b) depicts the macroscopic fracture of $\mathbf{CA}^{\mathbf{A}}_{\varnothing 6}$, where the fracture is classified as **LGM** [28] (Laminate tensile failure laterally across the center of the hole. Cracks and delaminations may be present). Cracks were only observed in the region of the fracture. The fracture in $\mathbf{CA}^{\mathbf{A}}$ displayed transverse cracks along the entire test specimen and intense cracking in the final fracture region, showing that the hole concentrates damage only in this region (around the hole) in $\mathbf{CA}^{\mathbf{A}}_{\varnothing 6}$.

Macroscopic analysis of the mechanical fracture in $\mathbf{CA}^{\pm 45^{\circ}}_{\varnothing 6}$ (Fig. 11 (c)) displays high transverse strain (constriction) in the region near the final fraction. A certain “invasion” of aramid fibers was also observed at the hole. No significant damage was found along the test specimen, but delamination can be seen in the region of the fracture. The fracture mode is **AGM** [28] (laminate generally exhibits stress failure at the hole, but remnants of angle plies cross the lateral centerline of the hole. Cracks and delaminations may be present). Comparison with the $\mathbf{CA}^{\pm 45^{\circ}}$ fracture reveals that the hole influenced the characterisitcs of the macroscopic fracture, given that aramid fiber tearing in $\mathbf{CA}^{\pm 45^{\circ}}$ was more intense than for $\mathbf{CA}^{\pm 45^{\circ}}_{\varnothing 6}$. The hole concentrated damage in the region around the final fracture, which caused intense strain in the area, making the hole elliptic before the final fracture.

3.10. Residual properties and failure criteria: *PSC* and *ASC*

An assessment of residual properties, that is, the capacity of retaining the properties of tensile strength and Young's modulus for the three loading directions in the proposed laminates (**CGL** and **CAL**), according to Eqs. (1) and (2), is found in Table 4. Table 4 shows that **CGL** specimens, with orientation in the direction of the carbon fiber, showed less capacity to retain tensile strength (55%), while for Young's modulus the lower capacity was for specimens with glass fiber in the direction of loading. The specimens with glass fiber and carbon at 45° to the loading direction exhibited better retention for both properties, and $\mathbf{CG}^{\pm 45^{\circ}}_{\varnothing 6}$ obtained 72% retention of tensile strength. Young's modulus showed superiority for the case of a hole over the original condition, that is, the fact that Young's modulus of $\mathbf{CG}^{\pm 45^{\circ}}_{\varnothing 6}$ is slightly higher than that of $\mathbf{CG}^{\pm 45^{\circ}}$ can also be explained by the influence of the hole on the fracture, given that $\mathbf{CG}^{\pm 45^{\circ}}$ displayed high constriction (strain perpendicular to the loading direction) and significant bending of the specimens. These characteristics were not observed in $\mathbf{CG}^{\pm 45^{\circ}}_{\varnothing 6}$, showing that the presence of a hole relieved shear stress (given that the fibers were oriented at 45°).

Assessment of the residual properties of **CAL** demonstrates that the aramid fiber in the loading direction obtained the lowest retention for tensile strength (52%) and Young's modulus (61%), compared to retention of the properties of all the other specimens studied.

The specimens with carbon and aramid fibers oriented at 45° in relation to the loading direction displayed better retention capacity. The tensile strength of specimens with a hole was higher than that of specimens in the original condition, given that $\mathbf{CA}^{\pm 45^{\circ}}$ exhibited no load support in the shear stage, whereas $\mathbf{CA}^{\pm 45^{\circ}}_{\varnothing 6}$ showed slight load support capacity (since strain is concentrated in the region around the hole), relieving shear stress. With respect to Young's modulus, $\mathbf{CA}^{\pm 45^{\circ}}_{\varnothing 6}$ retained 96% of the property, the difference being lower than the standard deviation of the modulus. It is important to underscore that the use of the geometric K for residual strength (RS) values greater than 1.0 ($\mathbf{CA}^{\pm 45^{\circ}}_{\varnothing 6}/\mathbf{CA}^{\pm 45^{\circ}}$) led to non-validated characteristic distances d_0 and a_0, given that the fracture stress of the specimen with no discontinuity was close to that of that with discontinuity, that is, the influence of concentrated stress was minimized, which contrasts with failure theories.

Thus, the purpose is to determine these distances semi-empirically, that is, considering the **PSC** and **ASC** failure models and the RS values for both **CGL** and **CAL** configurations (with a hole). For the semi-empirical calculation of d_0 and a_0, the value of $K = 2.58$ for hole specimens was used and determined solely in relation to the geometry of the specimen [4,38], since $K = 3.0$ could not be used because both configurations were orthotropic. The values of RS and geometric K were used to calculate the characteristic distances using **PSC** (Eqs. (3) and (4)) and **ASC** (Eqs. (4) and (5)) failure theories. The values of the characteristic distances for both criteria are listed in Table 4. The semi-empirical values of the characteristic distances for the specimens show that the use of the simplified value of K, that is, determined solely in relation to the geometry, exhibited good agreement mainly regarding the percentage of the region of stress concentration for the **PSC** and **ASC** theories, for both **CGL** and **CAL** composite laminates.

Table 4
Values of d_0 and a_0 of **CGL** and **CAL** specimens.

Configuration	Residual Strength	Residual Modulus	Stress concentration factor (K)	**PSC** d_0 (mm)	**ASC** a_0 (mm)
$\mathbf{CG}^{\mathbf{C}}_{\varnothing 6}/\mathbf{CG}^{\mathbf{C}}$	0.55	0.78	2.58	0.96	2.25
$\mathbf{CG}^{\mathbf{G}}_{\varnothing 6}/\mathbf{CG}^{\mathbf{G}}$	0.60	0.74	2.58	1.24	3.11
$\mathbf{CG}^{\pm 45^{\circ}}_{\varnothing 6}/\mathbf{CG}^{\pm 45^{\circ}}$	0.72	1.13	2.58	2.04	6.35
$\mathbf{CA}^{\mathbf{C}}_{\varnothing 6}/\mathbf{CA}^{\mathbf{C}}$	0.64	0.75	2.58	1.48	4.00
$\mathbf{CA}^{\mathbf{A}}_{\varnothing 6}/\mathbf{CA}^{\mathbf{A}}$	0.52	0.61	2.58	0.81	1.80

4. Conclusions

A number of conclusions can be drawn based on the results of this study:

- Laminates **CGL** and **CAL** are strongly influenced by anisotropy, especially specimens in the original condition and the characteristics of the final macroscopic fracture were significantly influenced by anisotropy and the hole, and are in accordance with mechanical behavior (stress/strain curve) obtained in the uniaxial tensile strength test;
- $\mathbf{CG^{C}}$ and $\mathbf{CG^{C}_{\varnothing 6}}$ exhibited bilinear behavior, which is atypical for most fiber-reinforced polymer composite laminates (impregnated with thermoset resins);
- The specimens with carbon fibers in the direction of load application, displayed the highest Young's moduli, in the following order: $\mathbf{CG^{C}} > \mathbf{CG^{C}_{\varnothing 6}} > \mathbf{CA^{C}}$ and all the species with fibers oriented at ±45° in relation to the applied load, showed a high strain rate, in the following decreasing order: $\mathbf{CG^{\pm 45^{\circ}}} > \mathbf{CA^{\pm 45^{\circ}}} > \mathbf{CG^{\pm 45^{\circ}}_{\varnothing 6}} > \mathbf{CA^{\pm 45^{\circ}}_{\varnothing 6}}$ and suffered intense constriction damage;
- In relation to the capacity to retain properties, specimens $\mathbf{CG^{C}_{\varnothing 6}/CG^{C}}$ and $\mathbf{CA^{C}_{\varnothing 6}/CA^{C}}$ exhibited lower RS, while $\mathbf{CG^{\pm 45^{\circ}}_{\varnothing 6}/CG^{\pm 45^{\circ}}}$ and $\mathbf{CA^{\pm 45^{\circ}}_{\varnothing 6}/CA^{\pm 45^{\circ}}}$ showed higher RS and RM. With respect to the values of the semi-empirical distances found in both failure criteria, when using *K*, determined solely in relation to the geometry of the specimens, good agreement was found for **PSC** and **ASC**.

Acknowledgements

The authors acknowledge Postgraduate Program in Materials Science and Engineering and Postgraduate Program in Mechanical Engineering by the access of their laboratories and CNPq for postdoctoral scholarships.

References

[1] Wan YZ, Lian JJ, Huang Y, Wang YL, Chen GC. Two-step surface treatment of 3D braided carbon/Kevlar hybrid fabric and influence on mechanical performance of its composites. Mater Sci Eng A 2006;429:304–11.
[2] Davoodi MM, Sapuan SM, Ahmad D, Aidy A, Khalina A, Jonoobi M. Effect of polybutylene terephthalate (PBT) on impact property improvement of hybrid kenaf/glass epoxy composite. Mater Lett 2012;67:5–7.
[3] Aji IS, Zainudin ES, Khalina A, Sapuan SM, Khairul MD. Studying the effect of fiber size and fiber loading on the mechanical properties of hybridized kenaf/PALF-reinforced HDPE composite. J Reinf Plast Compos 2011;30(6):546–53.
[4] Tinô SRL, Fontes RS, Aquino EMF. Theories of failure average stress criterion and point stress criterion in notched fiber-reinforced plastic. J Compos Mater 2014;48(21):2669–76.
[5] Kistaiah N, Udaya Kiran C, Ramachandra Reddy G, Sreenivasa Rao M. Mechanical characterization of hybrid composites: a review. J Compos Mater 2014;33(14):1364–72.
[6] Xia C, Yu J, Shi SQ, Qiu Y, Cai L, Wu HF, et al. Natural fiber and aluminum sheet hybrid composites for high electromagnetic interference shielding performance. Compos Part B 2017;114:121–7.
[7] Fiore V, Scalici T, Sarasini F, Tirilló J, Calabrese L. Salt-fog spray aging of jute-basalt reinforced hybrid structures: flexural and low velocity impact response. Compos Part B 2017;116:99–112.
[8] Dong C, Heshan A, Ranaweera-Jayawaedena Davies IJ. Flexural properties of hybrid composites reinforced by S-2 glass and T700S carbon fibres. Compos Part B 2012;43:573–81.
[9] Zhang J, Chaisombat K, Shuai HE, Wang CH. Hybrid composite laminates reinforced with glass/carbon woven fabrics for lightweight load bearing structures. Mater Des 2012;36:75–80.
[10] Pandya KS, Veerraju CH, Naik NK. Hybrid composites made of carbon and glass woven fabrics under quasi-static loading. Mater Des 2011;32:4094–9.
[11] Sayer M, Bektas NB, Demir E, Çallioğ lu H. The effect of temperatures on hybrid composite laminates under impact loading. Compos Part B 2012;43:2152–60.
[12] Batista ACM, Oliveira JFS, Aquino EMF. Structural degradation and mechanical fracture of hybrid fabric reinforced composites. Polym Eng Sci 2016;56:657–68.
[13] Valença SL, Griza S, Oliveira VG, Sussuchi EM, Cunha FGC. Evaluation of the mechanical behavior of epoxy composite reinforced with Kevlar plain fabric and glass/Kevlar hybrid fabric. Compos Part B 2015;70:1–8.
[14] Guermazi N, Haddar N, Elleuch K, Ayed HF. Investigations on the fabrication and the characterization of glass/epoxy, carbon/epoxy and hybrid composites used in the reinforcement and the repair of aeronautic structures. Mater Des 2014;56:714–24.
[15] Gemi L, Şahin ÖS, Akdemir A. Experimental investigation of fatigue damage formation of hybrid pipes subjected to impact loading under internal pressure. ComposPart B 2017;119:196–205.
[16] Hocheng H, Tsao CC. Effects of special drill bits on drilling-induced delamination of composite materials. Int J Mach Tool Manu 2006;46:1403–16.
[17] Ye L, Afaghi-Khatibi A, Lawcock G, Mai Y-W. Effect of fibre/matrix adhesion on residual strength of notched composite laminates. Compos Part A 1998:1525–33.
[18] Tinô SRL, Aquino EMF. Notched GFRP: anisotropy, residual strength, and fracture characteristics. J Reinf Plast Compos 2011;31(1):29–40.
[19] Hwan CL, Tsai KH, Chiu CH, Huang YS. Strength prediction of woven hybrid composite laminates each with a center hole. J Compos Mater 2013;0(0):1–8.
[20] Morais AB. Open-hole tensile strength of quasi-isotropic laminates. Compos Sci Technol 2000;60:1997–2004.
[21] Hallett SR, Green BG, Jiang WG, Wisnom WR. An experimental and numerical investigation into the damage mechanisms in notched composites. Compos Part A 2009;40:613–24.
[22] Mollenhauer D, Iarve EV, Kim R, Langley B. Examination of ply cracking in composite laminates with open holes: a moiré interferometric and numerical study. Compos Part A 2006;37:282–94.
[23] Tan SC. Stress concentrations in laminated composites. Lancaster: Technomic; 1994.
[24] Bhattacharyya D, Horrigan DPW. A study of hole drilling in kevlar composites. Compos Sci Technol 1998;58:267–83.
[25] ASTM D 792 Standard test methods for density and specific gravity (relative density) of plastics by displacement. 2008.
[26] ASTM D 3171 Standard test methods for constituent content of composite materials. 2009.
[27] ASTM D3039 Standard test methods for tensile properties of polymer matrix composites. 2008.
[28] ASTM D5766/D5766M Standard test method for open-hole tensile strength of polymer matrix composite laminates. 2011.
[29] Santos CC. Propriedades Mecânicas Residuais após Incêndio de Betões Normais. doctoral thesisvol. 235. Coimbra-Portugal: Faculdade de Ciências e Tecnologia-Universidade de Coimbra; 2012.
[30] Awerbuch J, Madhukar MS. Notched strength of composite laminates: predictions and experiments – a review. J Reinfor Plast Compos 1985:159.
[31] Nuismer RJ, Whitney JM. Uniaxial failure of composite laminates containing stress concentration. In: Fracture mechanics of composites. ASTM STP 593-American Society of testing and materials; 1975. p. 117–42.
[32] Wu H-C, Mu B. On stress concentrations for isotropic/orthotropic plates and cylinders with a circular hole. Comp Part B 2003;34:127–34.
[33] Matthews FL, Rawlings RD. Composite materials: engineering and science. NW Boca Raton: CRC; 1994.
[34] Daniel IM, Ishai O. Engineering mechanics of composite materials. 2th ed. Oxford University Press; 2006.
[35] Bergmann T, Heimbs S, Maier M. Mechanical properties and energy absorption capability of woven fabric composites under ±45° off-axis tension. Compos Struct 2015;125:362–73.
[36] ASTM D D3518/D3518M–13 Standard test method for in-plane shear response of polymer matrix composite materials by tensile test of a ±45° laminate. 2013.
[37] Toubal L, Karama M, Lorrain B. Stress concentration in a circular hole in composite plate. Compos Struct 2005;68:31–6.
[38] Shigley JE, Mischke CR. In: Mechanical engineering design. fifth ed. USA: McGraw-Hill Inc; 2002.